Optics Letters

Harmonic suppression gratings for soft X-ray monochromators

Kenneth A. Goldberg,[1,*] Harold S. Barnard,[1] Sooyeon Park,[1] Eric M. Gullikson,[2] and Dmitriy L. Voronov[1]

[1]Advanced Light Source, Lawrence Berkeley National Laboratory, Berkeley, California 94720, USA
[2]Center for X-ray Optics, Lawrence Berkeley National Laboratory, Berkeley, California 94720, USA
*kagoldberg@lbl.gov

Received 12 December 2025; revised 10 February 2026; accepted 17 February 2026; posted 17 February 2026; published 11 March 2026

We describe an approach to harmonic suppression in soft X-ray monochromators by engineering the reflection grating's diffraction pattern to approximate a sinusoidal amplitude. At synchrotron and free-electron laser sources, X-ray beamlines powered by insertion devices produce a spectrum containing harmonic photon energies that can couple unwanted light into experiments. Beamlines in the soft X-ray energy range (100 eV to 2 keV) commonly employ energy-filtering elements to suppress these harmonics. Available approaches tend to be inefficient, significantly reducing the transmitted power. We show that with pseudo-grayscale binary halftone patterns, gratings can approximate a sinusoidal amplitude and suppress higher diffraction orders. Prototype demonstrations of lithographically fabricated gratings were conducted on a soft X-ray beamline with photon energies of 110 eV and 330 eV. Relative to a square-wave amplitude grating, the third-harmonic intensity was reduced by a factor of 9.0 with a first-order efficiency reduction of 38%. © 2026 Optica Publishing Group. All rights, including for text and data mining (TDM), Artificial Intelligence (AI) training, and similar technologies, are reserved.

https://doi.org/10.1364/OL.587366

Beamlines at synchrotron and free-electron laser light sources are used for a wide variety of spectroscopy applications [1,2]. In the soft X-ray energy range (100 eV to 2 keV), sub-micron focused beam widths and higher spatial resolutions provide experimental systems with important capabilities in material science. High photon-energy resolution enables these tools to probe chemical states, band structures, and other material properties with great sensitivity [3,4].

High-flux undulator and wiggler insertion-device (ID) sources are periodic magnet arrays that use adjustable field strength to control the deflection of relativistic electron beams and continuously tune the emitted photon energy over a range. These sources also produce a spectrum of harmonics at integer multiples of the fundamental photon energy ($E_n = nE_1$) [5]. While each harmonic has an angular spectrum close to the central axis, for many types of IDs, the odd-harmonics are brightest on-axis: they co-propagate with the fundamental beam. While these harmonics are often used to access higher photon energies, their presence overlapping the fundamental-energy beam must be suppressed in many applications.

Grating-based monochromators are the most common spectral filtering approach for soft X-ray beamlines. Illuminated at glancing angles of incidence (up to several degrees), reflection gratings are typically mechanically ruled or lithographically patterned to have periodic surface structures on a micron or submicron scale (i.e., hundreds to thousands of lines per mm). The grating line spacing can be uniform, or it can be variable, to focus diffracted light holographically [6–8]. Reflection gratings can be patterned on flat or curved surfaces as the beamline optical system design requires, but in all cases, the principle is the same: downstream filtering preferentially transmits or rejects the various orders.

A central challenge arises in filtering harmonics with high on-axis power. The in-plane reflection grating equation that describes the diffraction conditions for any local point on the grating surface is [9]:

$$d\,(\cos\theta_i - \cos\theta_r) = n\lambda. \tag{1}$$

The local grating pitch is d, θ_i and θ_r are the incident and reflected glancing angles, n is the integer diffraction order, and λ is the wavelength, related to the photon energy by $E = hc/\lambda$. Cursory inspection of this equation shows that the n-th diffraction order ($n > 1$) of the n-th energy harmonic ($\lambda_n = \lambda_1/n$) will diffract at the same θ_r angle as the $n = 1$ fundamental. Therein lies the problem. For a fundamental energy of 110 eV, the 1st-order diffracted beam will be overlapped by the 3rd order of 330 eV, the 5th order of 550 eV, and so forth.

Numerous available harmonic suppression strategies exploit the angle- and energy-dependent reflectivity, or the relative transmission of various materials. For example, Dietrich, Hunter, and others combined grating blaze angles and the energy-dependent critical angles of thin-film coatings to serve as an energy filter [10–12]. Waki and Harada suppressed higher energies with a rotating array of interchangeable mirror pairs [13,14]. A tunable, symmetric, three-mirror mechanism was described by Terminello, Frommherz, and others [15,16]; this approach is widely used. Within monochromators, Petersen and Dietz use reflection from the monochromator's pre-mirror to suppress higher photon energies [17,18], while Andronova *et al.* proposed that a pair of X-ray multilayer mirrors would provide sufficient filtering in many cases [19]. Quinn described the

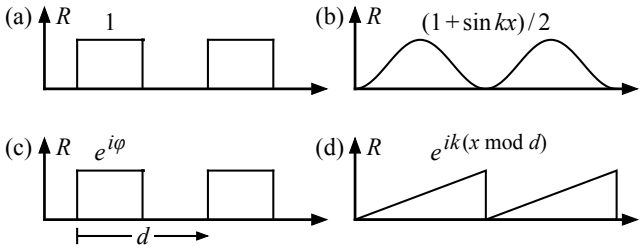

Fig. 1. Idealized grating models: (a) binary amplitude, (b) sinusoidal amplitude, (c) binary phase, (c) blazed.

common use of various thin-film transmission filters [20]. Each approach offers advantages that come at the cost of reduced throughput, added complexity, or reduced wavefront quality.

Distinct from these approaches, which all rely on energy-dependent material properties, we have engineered the reflective grating pattern itself to suppress unwanted harmonic content in the diffracted light. In this way, some first-order diffraction efficiency is traded for harmonic suppression. The approach derives from an examination of simplified grating models.

The reflected-diffracted angular spectrum and relative strengths of the diffracted orders can be predicted from the calculated field of the reflected beam using scalar diffraction theory [21]. (Partially coherent extensions can be made from this coherent-light understanding.) Define a grating's local spatial frequency as $k = 2\pi/d$. The grating's pattern, $c(x)$, describes the way it modulates the reflected light field.

The pattern can be decomposed into a complex Fourier series represented by the coefficients $\{c_n\}$. Assuming uniform illumination, these coefficients will correspond to the relative complex amplitudes of the diffracted orders. The Fourier coefficients can be calculated with periodic boundary conditions.

$$c_n = \frac{1}{d}\int_0^d c(x)\, e^{-iknx}\, dx. \tag{2}$$

The power in each order is proportional to $|c_n|^2$. Textbook exercises reveal the Fourier coefficients for two cases that are important to this discussion: (1) a binary amplitude pattern with equal lines and spaces (*square* grating), and (2) sinusoidal amplitude.

$$\text{binary amplitude:}\quad |c_n| = \begin{cases} \frac{1}{2}, & n = 0 \\ \frac{1}{\pi|n|}, & n \text{ is odd} \\ 0, & n \text{ is even,} \end{cases} \tag{3a}$$

$$\text{sinusoidal amplitude:}\quad |c_n| = \begin{cases} \frac{1}{2}, & n = 0 \\ \frac{1}{4}, & n = \pm 1 \\ 0, & \text{otherwise.} \end{cases} \tag{3b}$$

Two additional patterns are commonly used. (3) Binary phase gratings reflect light with two phase-shift values (arising from optical path length variation). (4) Blazed gratings have a sawtooth profile, and behave in reflection as a type of phase grating, modifying the path length with a linear ramp and 2π steps. Figure 1 shows idealized models of these gratings.

Among these four grating types, the sinusoidal amplitude grating suppresses higher-order diffraction beyond $|n| = 1$. Equation (3b) shows that all higher coefficients are zero. However, fabricating a continuous, sinusoidal-reflection-amplitude pattern for X-rays at relevant length scales is an exceptional challenge. (Ideal blazed gratings would also suppress higher orders, but shadowing from the oblique illumination leads to higher-ordered diffraction.)

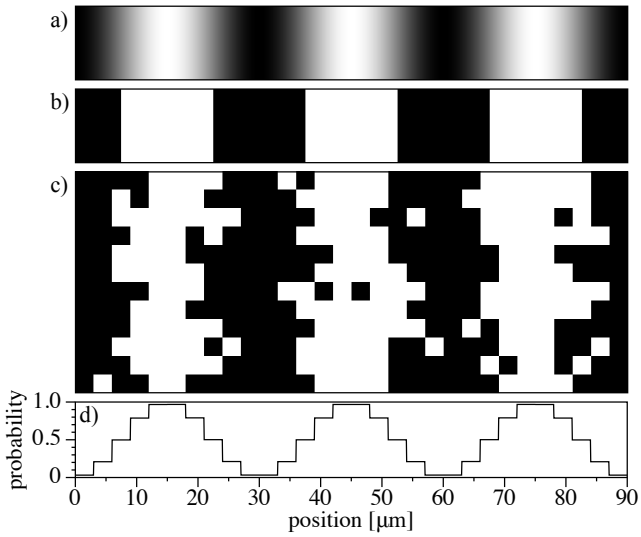

Fig. 2. Three reflective grating designs with pitch $d = 30\,\mu$m. (a) Sinusoidal amplitude pattern ranging from 0 to 1. (b) Equal line-space binary amplitude pattern. (c) Detail of the pixelated halftone with a 3 μm pixel pitch, based on a discretized sinusoidal probability function derived from (a). Plot (d) shows the vertically integrated and normalized halftone pattern's amplitude, column by column. As shown, the gratings would be illuminated in the horizontal direction.

In this work, we approximate sinusoidal patterns with pseudo-grayscale halftones. Diffraction into the far-field domain coherently combines the contributions of many pixelated elements to approximate the analogous, continuous pattern.

Figure 2 shows three grating patterns in detail over three cycles. The binary square-wave pattern (Fig. 2(b)) is the simplest discretization of the sinusoidal pattern (Fig. 2(a)). The halftone pattern (Fig. 2(c)), pixelated on a square grid with 10 pixels per cycle, is defined point-by-point, using uniform random numbers on [0,1) with the sinusoidal pattern serving as a probability function that determines whether each pixel is *white* or *black*.

A number of authors have pursued similar approaches, including some for soft X-ray applications that have inspired this work. Most such demonstrations have been conducted on transmission gratings. Zhao produced a square-grid random halftone [22] akin to the grating described here, but in transmission. Cao described a binary transmission grating with sinusoidally shaped openings [23], which Zhang transformed into a *zigzag* [24], and Chen later reproduced as a reflective multilayer for tender X-rays [25]. Zhao and also Kuang showed a halftone approach in transmission that shifted a line or space segments longitudinally without breaking [22,26]. Gao and then Yang broke the pattern periodicity with random, sinusoidally modulated, whole-line longitudinal displacements [27,28]. Zhang and then Chen designed photon-sieve gratings made from pinholes [29,30].

We created an array of prototype gratings with 30 μm pitch using contact-printing lithography and deep etching. (These periods are somewhat larger than what is commonly used for soft X-ray gratings: 100 nm to 20 μm.) On a 100 mm, prime-grade silicon wafer, each gratings covers a 5 mm by 30 mm area. Designed for illumination at 0.5° incidence, only the un-etched

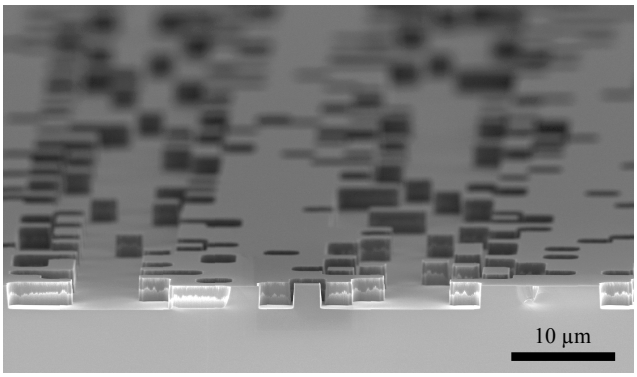

Fig. 3. Scanning electron microscope micrograph of the halftone grating with 30 µm pitch, 3 µm pixels, and a 2.5 µm approximate etch depth. The wafer was cleaved to provide this inspection.

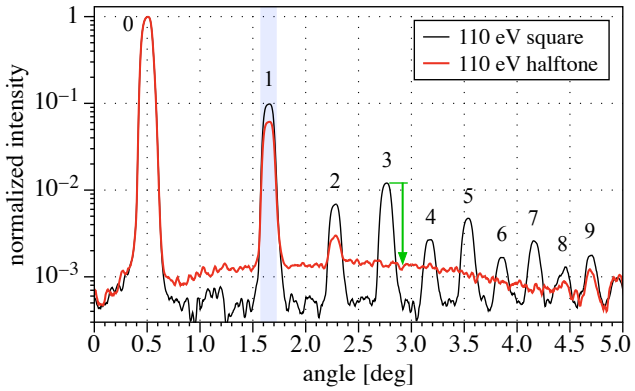

Fig. 4. Binary amplitude grating diffraction measurements, comparing square-wave (black) and sinusoidal halftone (red). Gratings are illuminated with 110 eV soft X-ray light at 0.5 °incidence . The positions of the various grating orders are labeled, with the blue stripe identifying the first-order.

top surface of the pattern reflects X-ray light [31]. A scanning electron microscope image of a halftone grating is shown in Fig. 3. The minimum feature size in this prototype was constrained by fabrication limits to several microns; however, the edge placement was defined on a 50 nm grid.

Gratings were measured with soft X-ray light at the Advanced Light Source's Beamline 6.3.2 [32]. The monochromatic beam ($E/\Delta E = 1000$) has a spot size of 120 × 40 µm at focus. At 0.5 ° incidence, the beam footprint is approximately 4.584 mm long, illuminating 152 periods of the grating. Laterally, the beam covers approximately 40 3-µm pixels.

The angular patterns of the reflected/diffracted light were measured in the plane of incidence using a photodiode restricted by a 0.5 mm pinhole, 240 mm from the grating. The pinhole subtends 2.08 mrad or 0.119 °. In 1001 points from 0 ° (grazing) to 5 °, the angular spectra reveal the diffracted order intensities.

Measurements of the square-wave grating and the sinusoidal halftone grating are shown in Fig. 4, with a photon energy of 110 eV, and Fig. 5, with 330 eV light, representing the third harmonic. Each measurement is normalized to the 0th-order (specular) peak intensity at ($\theta_r = 0.5$ °) to facilitate comparison.

These measurements demonstrate the halftone grating's suppression of higher orders: in particular, the 3rd-order reductions

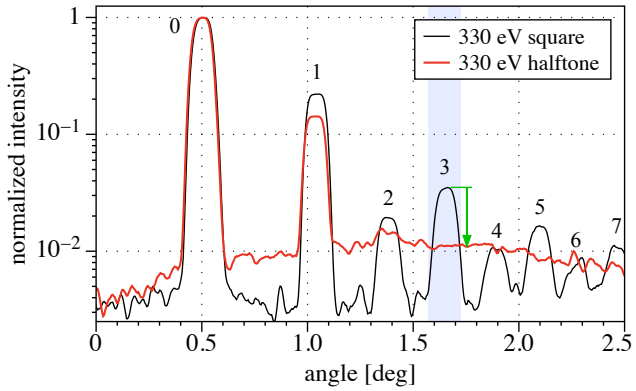

Fig. 5. Measurement of the same two gratings as Fig. 4, illuminated at 330 eV. The blue stripe identifies the first-order position for 110 eV and shows how the third order of 330 eV can overlap.

are called out with green arrows. Remember that our goal is to suppress the 3rd-order diffraction of the 3rd-harmonic energy.

At 110 eV, the normalized first-order peak intensities (at θ_r = 1.65 °) reach 0.098 for the square-wave and 0.061 (62%) for the halftone grating. Beyond first-order, small second-order peaks are visible. The halftone creates a low, scattered background of light over the measurement range. At the angle of third-order diffraction, the halftone intensity is 9.0× lower than the square-wave (0.0120 versus 0.00134).

For the 330 eV measurements near $\theta_r = 1.65$ °, the halftone's diffuse signal is 3.14× lower than the square-wave gratings' third-order intensity (0.0112 versus 0.00351), but importantly, it is 89× lower than the specular intensity. For comparison, the square wave's third-order intensity is 28.5× lower than the specular intensity.

In some beamlines, the overlapping of 2nd-order light is not negligible. Figure 4 shows a factor of 2.30 reduction of the 2nd-order diffraction intensity of 110 eV light. For measurements made with 220 eV light (not shown), the halftone grating reduces the 2nd-order power by only 6.70% relative to the square grating. Second-order and other even diffraction orders are already diminished by square-wave gratings (see Eq. (3a)). Residual power in these orders arises from pattern imperfections of deviations from the equal line-space target.

The high scattered-light background level is attributable to the low number of grating periods illuminated (~152). Illuminating hundreds or thousands of lines would more closely approximate the sinusoidal analog and reduce scattering.

So with this prototype, we find that relative to the square-wave amplitude grating, the halftone sacrifices 38% of the first-order power to gain a factor of 3.14 in third-order suppression. When compared to other inefficient or mechanically complex approaches to harmonic suppression (i.e., multiple reflections, angle-adjusting mirrors, various absorptive coatings), the use of harmonic-suppression gratings may be beneficial.

While this prototype demonstration achieves its objectives, we believe there is significant room for improvement with high-quality gratings in real-world conditions. First, our measured performance was limited by the number of lines we could illuminate in the beam footprint (approximately 152). X-ray monochromators commonly illuminate several thousand lines to achieve high spectral resolution. Second, with a square-grid halftone pattern, the performance is limited by the pixel

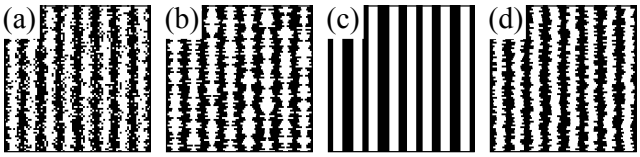

Fig. 6. Comparison of halftone pattern details. (a) Square grid with 10 pixels per period. (b) Sub-pixel symmetric edge positioning in one dimension. (c) Modulated line displacements. (d) Quasi-sinusoidal random displacements along the line.

size, or equivalently, the number of pixels per cycle. Separate measurements show that the performance of the halftone pattern improves as the total number of illuminated pixels increases. With a square-grid halftone pattern, the performance limit is not actually that of a *continuous* sinusoidal amplitude grating. Rather, with N pixels per cycle, the performance approaches a sine function discretized to N steps. This fact is evident in the presence of 9th-order and 10th-order peaks, visible in Fig. 4.

Alternative halftone patterns that break the square-grid pixel layout, or optimize the pattern toward other metrics [33], offer different ways to suppress harmonics, if they are achievable within fabrication capabilities. Figure 6 compares the square-grid halftone (Fig. 6(a)) to a grating defined on a sub-pixel grid in the direction of propagation (Fig. 6(b)). This pattern yields a closer approximation of the continuous sinusoidal amplitude. Here, a set of N horizontal pattern segments is created to match the target amplitude when integrated. Their positions along the line are randomly shuffled to break the periodicity and smooth the resultant diffraction downstream.

Gao [27] and Yang's [28] methods of modulated line displacements (Fig. 6(c)) eliminate lateral scattering. Zhao [22] and Kuang's [26] longitudinal line displacements in narrow segments (Fig. 6(d)) approximate sinusoidal amplitude while preserving either constant line or space width.

Generally, monochromator gratings with halftone patterns, or those with any non-uniform structure in the non-dispersive direction, may require two-dimensional spatial filtering in the monochromator's exit slit plane to reduce scattered light.

It should also be possible to incorporate the halftone pattern concept into lithographically patterned phase gratings with shallow binary step heights designed to achieve a π phase shift (or $\lambda/2$ path-length change) in the alternating regions. Blazed gratings may also benefit from this approach. This may be important for optimizing efficiency, and also in consideration of sources with power densities high enough to damage lamellar amplitude gratings.

This approach is extendable into the extreme ultraviolet and vacuum ultraviolet ranges, where larger grating pitch values grant an opportunity for finer sub-period pattern control.

Funding. Director, Office of Science, Office of Basic Energy Sciences of the U.S. Department of Energy (DE-AC02-05CH11231).

Acknowledgment. We appreciate experiment support from Sabria Hinton of California State University, East Bay and the LBNL ASPIRES Internship program. We are grateful for insightful comments from Antoine Islegen-Wojdyla, Nicolás Smith, and Howard Padmore.

Disclosures. The authors declare no conflicts of interest.

Data availability. Data underlying the results presented in this paper are not publicly available at this time but may be obtained from the authors upon reasonable request.

REFERENCES

1. L. J. P. Ament, M. van Veenendaal, T. P. Devereaux, *et al.*, Rev. Mod. Phys. **83**, 705 (2011).
2. D. A. Shapiro, R. Celestre, B. Enders, *et al.*, Microsc. Microanal. **24**, 8 (2018).
3. A. Bostwick, T. Ohta, T. Seyller, *et al.*, Nat. Phys. **3**, 36 (2007).
4. W. Yang, X. Liu, R. Qiao, *et al.*, J. Electron Spectrosc. Relat. Phenom. **190**, 64 (2013).
5. K.-J. Kim, Z. Huang, and R. Lindberg, *Synchrotron Radiation and Free-Electron Lasers* (Cambridge University Press, 2017).
6. M. C. Hettrick and S. Bowyer, Appl. Opt. **22**, 3921 (1983).
7. M. C. Hettrick and J. H. Underwood, in *AIP Conference Proceedings* (AIP, 1986), Vol. **147**, p. 237.
8. R. Reininger and A. de Castro, Nucl. Instrum. Methods Phys. Res. A **538**, 760 (2005).
9. M. Born and E. Wolf, *Principles of Optics*, 6th ed. (Pergamon Press, 1980), Chap. 8.6.1, p. 403.
10. H. Dietrich and C. Kunz, Rev. Sci. Instrum. **43**, 434 (1972).
11. W. R. Hunter and J. C. Rife, Appl. Opt. **23**, 293 (1984).
12. J. C. Rife, W. R. Hunter, and R. T. Williams, Nuclear Inst. Methods Phys. Res., A **246**, 252 (1986).
13. I. Waki, Y. Hirai, A. Momose, *et al.*, Rev. Sci. Instrum. **60**, 2072 (1989).
14. T. Harada, Nucl. Inst. Methods Phys. Res. A **291**, 179 (1990).
15. L. J. Terminello, A. B. McLean, A. Santoni, *et al.*, Appl. Phys. Rev. **61**, 1626 (1990).
16. U. Frommherz, J. Raabe, B. Watts, *et al.*, AIP Conf. Proc. **1234**, 429 (2010).
17. H. Petersen, Opt. Commun. **40**, 402 (1982).
18. E. Dietz, W. Braun, A. M. Bradshaw, *et al.*, Nucl. Inst. Methods Phys. Res. A **239**, 359 (1985).
19. N. V. Andronova, V. G. Kohn, and A. I. Chechin, Nucl. Inst. Methods Phys. Res. A **359**, 284 (1995).
20. F. M. Quinn, D. Teehan, M. MacDonald, *et al.*, J. Synchrotron Radiat **5**, 783 (1998).
21. J. W. Goodman, *Introduction to Fourier Optics*, 2nd ed. (McGraw-Hill, 1996).
22. M. Zhao, X. L. Zhu, C. Q. Xie, *et al.*, Opt. Eng. **47**, 058001 (2008).
23. L. F. Cao, E. Förster, A. Fuhrmann, *et al.*, Appl. Phys. Lett. **90**, 053501 (2007).
24. H. P. Zang, C. K. Wang, Y. L. Gao, *et al.*, Appl. Phys. Lett. **100**, 111904 (2012).
25. J. Chen, L. Wei, Z. Yang, *et al.*, J. Opt. Soc. Am. A **37**, 1008 (2020).
26. L. Y. Kuang, L. F. Cao, X. L. Zhu, *et al.*, Opt. Lett. **36**, 3954 (2011).
27. N. Gao and C. Xie, Opt. Lett. **36**, 4251 (2011).
28. Z. Yang, Q. Zhang, J. Wang, *et al.*, Chin. Phys. B **25**, 054209 (2016).
29. Q.-Q. Zhang, L. Wei, Z.-H. Yang, *et al.*, Chin. Phys. B **23**, 044215 (2014).
30. Y. Chen, L. Wei, F. Qian, *et al.*, Chin. Phys. B **27**, 024101 (2018).
31. K. A. Goldberg, D. Bryant, A. Wojdyla, *et al.*, Opt. Lett. **45**, 4694 (2020).
32. J. H. Underwood and E. M. Gullikson, Proc. SPIE **3331**, 52 (1998).
33. P. Stucki, Proc. SPIE **1670**, 26 (1992).

198.129.215.56 2026-03-11 12:35:2